

# SFP: Real-World Scene Recovery Using Spatial and Frequency Priors

Yun Liu<sup>1</sup>, Tao Li<sup>1</sup>, Cosmin Ancuti<sup>2</sup>, Wenqi Ren<sup>3</sup>, Weisi Lin<sup>4</sup>

<sup>1</sup>College of Artificial Intelligence, Southwest University

<sup>2</sup>Faculty of Electronics and Telecommunications Engineering, Universitatea Politehnica Timisoara

<sup>3</sup>School of Cyber Science and Technology, Shenzhen Campus, Sun Yat-sen University

<sup>4</sup>College of Computing and Data Science, Nanyang Technological University

## Abstract

Scene recovery serves as a critical task for various computer vision applications. Existing methods typically rely on a single prior, which is inherently insufficient to handle multiple degradations, or employ complex network architectures trained on synthetic data, which suffer from poor generalization for diverse real-world scenarios. In this paper, we propose **Spatial and Frequency Priors (SFP)** for real-world scene recovery. In the spatial domain, we observe that the inverse of the degraded image exhibits a projection along its spectral direction that resembles the scene transmission. Leveraging this spatial prior, the transmission map is estimated to recover the scene from scattering degradation. In the frequency domain, a mask is constructed for adaptive frequency enhancement, with two parameters estimated using our proposed novel priors. Specifically, one prior assumes that the mean intensity of the degraded image's direct current (DC) components across three channels in the frequency domain closely approximates that of each channel in the clear image. The second prior is based on the observation that, for clear images, the magnitude of low radial frequencies below 0.001 constitutes approximately 1% of the total spectrum. Finally, we design a weighted fusion strategy to integrate spatial-domain restoration, frequency-domain enhancement, and salient features from the input image, yielding the final recovered result. Extensive evaluations demonstrate the effectiveness and superiority of our proposed SFP for scene recovery under various degradation conditions.

## 1. Introduction

Images captured under challenging conditions, such as haze, sandstorm, and underwater scenarios, suffer from significant quality degradation in terms of contrast, color fidelity, and overall visibility, which negatively affects the accuracy of downstream applications. Therefore, scene recovery, which aims to restore clear and visually faithful im-

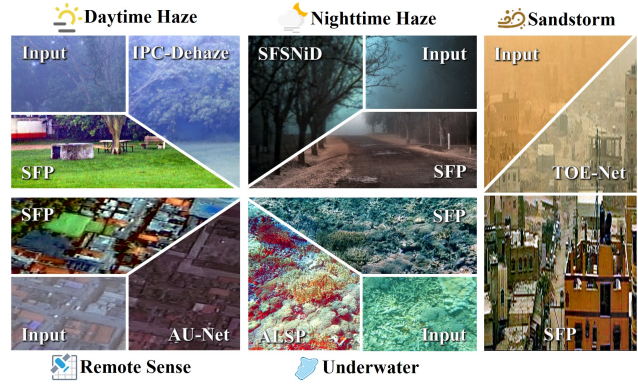


Figure 1. Examples of scene recovery under different degradation conditions, including daytime/nighttime haze, sandstorm, remote sensing, and underwater scenarios.

ages, is crucial for ensuring the reliability of vision-based systems in real-world applications.

Existing methods can generally be categorized into two groups: prior-based methods and learning-based methods. Prior-based methods [15, 19, 20, 24, 30, 50, 56, 58], such as DCP [15], MRP [50], HLRP [58], and SLP [30], typically rely on physical models and explore effective priors based on statistical observations to estimate scene transmission. However, these priors are specifically designed for a single task and are ineffective when dealing with multiple degradations. More recently, several priors such as ROP [31, 32] and ALSP [17] have been proposed for scene recovery under diverse degradation scenarios. However, the enhancement performance of these methods across various real-world scenarios still leaves room for improvement, primarily because single-domain priors fail to provide sufficient adaptability to cross-domain degradations.

Benefiting from advances in deep learning, a variety of networks [5, 6, 8, 9, 12, 28, 33, 39, 42, 44–46, 48] have been developed to address diverse image degradations. Early architectures are typically designed for a single task; for instance, DehazeNet [5], KA-Net [41], IPC-Dehaze [12], and SFSNiD [8] focus specifically on daytime/nighttime haze

removal. Recent methods, such as ERA-Net [33], MPMF-Net [46], IDB [28], UniRestore [6], and AdaIR [9] focus on all-in-one image restoration, aiming to simultaneously handle multiple types of degradations. However, learning-based approaches generally demand substantial computational resources. Moreover, although these methods perform well on synthetic data, their generalization to real-world degraded scenes remains limited due to the lack of large-scale paired datasets.

In order to adapt to diverse real-world degradation scenarios without relying on large-scale datasets or extensive computational resources, we propose a novel framework, called **Spatial and Frequency Priors (SFP)**, for real-world scene recovery. In the spatial domain, a new spatial-domain prior is proposed to estimate the transmission map by projecting the inverted input image onto the spectral direction, and the spatial-domain restoration is then obtained by inverting the ASM. In the frequency domain, two frequency-domain priors are developed based on the statistical distribution characteristics of low-frequency components in clear and degraded images, which are used to construct an adaptive mask for enhancing the degraded image in the frequency space. Finally, we introduce a weighted fusion strategy to integrate effective features from the spatial-domain restoration, frequency-domain enhancement, and the input image, yielding the final recovered result. Compared with existing prior- and learning-based methods, our SFP adapts well to diverse real-world degradations and achieves promising results, as illustrated in Figure 1. Overall, our main contributions are summarized as follows:

- We propose a novel real-world scene recovery framework using spatial and frequency priors. Different from traditional methods that rely on a single prior or domain, our SFP framework simultaneously addresses degradations in both spatial and frequency domains, improving scene recovery performance.
- We propose a spatial domain prior and two frequency-domain priors. The spatial prior leverages spectral properties to project the inverted degraded image onto the spectral direction, thereby approximating the scene transmission. The frequency priors focus on the direct current (DC) components and low radial frequencies to construct an adaptive mask, thereby enhancing the low-frequency characteristics that are primarily affected by degradations.
- Experiments on real-world datasets demonstrate that our SFP achieves superior performance, consistently yielding excellent results for various challenging tasks, including daytime/nighttime dehazing, underwater enhancement, remote sensing, and sandstorm image restoration.

## 2. Related Work

**Prior-based Methods.** Based on physical imaging models, numerous priors have been proposed to solve the ill-

posed inverse problem. The most representative one is the widely recognized DCP [15], assuming that in most non-sky regions, at least one color channel exhibits near-zero intensities, which allows the transmission to be estimated. Subsequently, CAP [56] assumes that pixel brightness and saturation vary significantly with haze concentration and further constructs a linear model for scene depth estimation. GCP [19] modifies gamma correction as a preprocessing step based on the observation that inverted low-light images resemble hazy images. RLP [20] exhibits a quasi-linear relationship between the average pixel intensities in hazy and corresponding haze-free regions. SLP [30] derives a linear relationship between the saturation component and the reciprocal of the brightness component. Despite providing effective dehazing performance, the aforementioned priors are limited in other degradation scenarios, such as nighttime haze. To achieve nighttime dehazing, Zhang et al. [50] propose a new prior named MRP to estimate the varying ambient illumination, based on the observation that daytime haze-free image patches often have high-intensity pixels in each color channel. In addition, variation priors, such as UVRM [35] and VNDHR [36], are specifically designed for nighttime haze removal to regularize the model. For underwater conditions, HLRP [58] introduces a variational Retinex model to enhance degraded images. These approaches achieve good results for their respective tasks; however, they fail to generalize to other degradation scenarios. To simultaneously overcome multiple challenging degradations, Liu et al. [31, 32] propose a rank-one prior (ROP) based on an intensity projection strategy to tackle daytime haze, sandstorms, and underwater conditions. More recently, ALSP [17] introduces the ambient light similarity metric and leverages the relationship between transmission and this metric for scene recovery. Nevertheless, their scene recovery performance in real-world scenarios remains limited, as they primarily consider single-domain degradations. In contrast, our SFP jointly exploits spatial and frequency priors for effective scene recovery under diverse degradations.

**Learning-based Methods.** Leveraging the powerful non-linear modeling capability of deep learning, several network architectures [5, 8, 11, 12, 39, 42, 45] are designed for a single degradation task. For instance, DehazeNet [5] learns to predict transmission maps directly from hazy inputs. Furthermore, KA-Net [11] and IPC-Dehaze [12] are developed to improve generalization for real-world dehazing. However, they are ineffective for nighttime hazy scenes owing to feature differences between daytime and nighttime hazy images. To achieve challenging nighttime dehazing, SF-SNiD [8] is for nighttime dehazing. In addition, EMPF-Net [45] and MABDT [39] focus on remote sensing degraded scenes. Recently, several all-in-one image restoration networks [9, 28, 33, 46, 48] have been proposed to han-

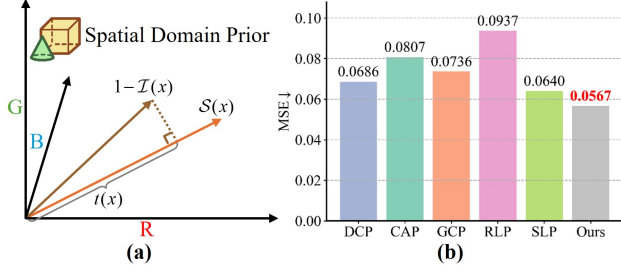


Figure 2. Illustration of our spatial-domain prior. (a) Schematic diagram of approximating the transmission map  $t(x)$  by projecting  $1 - \mathcal{I}(x)$  onto the spectral direction  $\mathcal{S}(x)$ . (b) Comparison of MSE deviations between estimated and ground-truth transmissions for various priors on the Haze4K test set.

degrade multiple degradations. Wen et al. [46] propose MPMF-Net, which leverages multi-axis prompt learning and multi-dimension feature interaction to restore weather-degraded images. AdaIR [9] mines both spatial and frequency domain information to address different types of degradations. Despite their impressive performance on simulated degraded images, learning-based approaches typically exhibit limited generalization to real-world scenes, primarily due to domain discrepancies. Moreover, data-driven methods require large-scale datasets for training and considerable computational resources.

### 3. Spatial and Frequency Priors

#### 3.1. Spatial-Domain Prior

The widely used atmospheric scattering model (ASM) [38] for describing the scene scattering process is expressed as:

$$\mathcal{I}(x) = \mathcal{J}(x) \circ t(x) + \mathcal{A} \circ (1 - t(x)), \quad (1)$$

where  $\circ$  denotes the Hadamard product.  $\mathcal{I}(x)$  and  $\mathcal{J}(x)$  represent the degraded image and the corresponding clear image, respectively.  $t(x)$  stands for the medium transmission, and  $\mathcal{A}$  indicates the global atmospheric light. Owing to the ill-posed nature of model inversion, a novel spatial-domain prior that accounts for spectral properties is proposed to estimate scene transmission.

The spectral direction represents color variations within an image and can be approximately modeled as the gradients of the three channels, which capture the rate of intensity change across spatial locations. Accordingly, the spectral direction  $\mathcal{S}(x)$  is defined as follows:

$$\mathcal{S}(x) = \frac{\sum_{x' \in \Omega(x)} \frac{(\nabla \mathcal{I}_{\mathcal{R}}(x'), \nabla \mathcal{I}_{\mathcal{G}}(x'), \nabla \mathcal{I}_{\mathcal{B}}(x'))}{\|\nabla \mathcal{I}(x')\|}}{|\Omega(x)|}, \quad (2)$$

where  $\mathcal{R}$ ,  $\mathcal{G}$ , and  $\mathcal{B}$  denote the color channels,  $\Omega(x)$  is the local patch centered at  $x$ , and  $\|\cdot\|$  is the modulus operation.

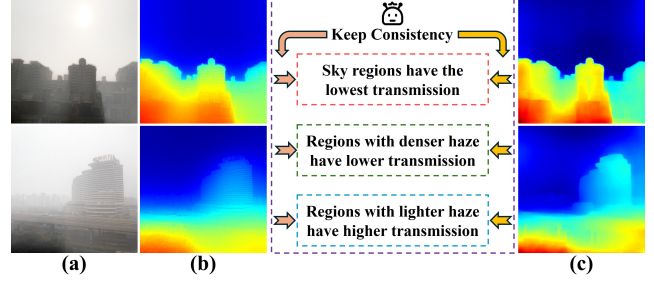


Figure 3. The projection of the inverted degraded image  $1 - \mathcal{I}(x)$  onto the spectral direction  $\mathcal{S}(x)$  closely resembles the ground-truth scene transmission. (a) Degraded images. (b) Transmission maps estimated by our spatial-domain prior. (c) Ground-truth transmission maps.

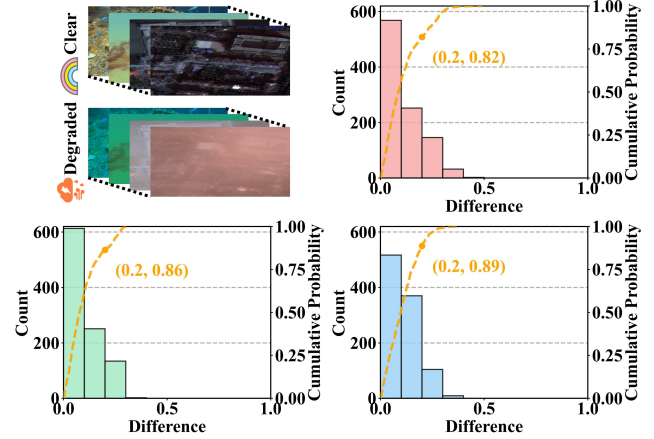


Figure 4. Statistical distributions of the absolute differences between the normalized DC component ( $DC \in [0, 1]$ ) of each channel (e.g.  $\mathcal{R}$ ,  $\mathcal{G}$ ,  $\mathcal{B}$ ) in clear images and the mean DC value across the three channels of their corresponding degraded images, computed on 1000 degraded-clean image pairs. The yellow dashed curves (cumulative distributions) show that over 80% of image pairs have absolute differences below 0.2 in all three channels.

We observe that projecting the inverted degraded image  $1 - \mathcal{I}(x)$  onto  $\mathcal{S}(x)$  provides a close approximation of the scene transmission, as illustrated in Figure 2(a). Intuitively,  $1 - \mathcal{I}(x)$  quantifies a pixel’s deviation from atmospheric light, which monotonically decreases as haze increases, thereby capturing degradation-related information relevant for transmission estimation.

To verify this finding, we compute the mean squared error (MSE) to quantify the discrepancy between the estimated and ground-truth transmissions on the Haze4K test set [34], with the statistical results shown in Figure 2(b). The proposed spatial-domain prior achieves superior performance, yielding estimates with smaller deviations from the ground truth compared to several famous priors, e.g. DCP [15], CAP [56], GCP [19], RLP [20], and SLP [30]. Figure 3 shows that our spatial-domain prior yields transmission maps which remain consistent with the ground truth across regions of varying haze concentrations.



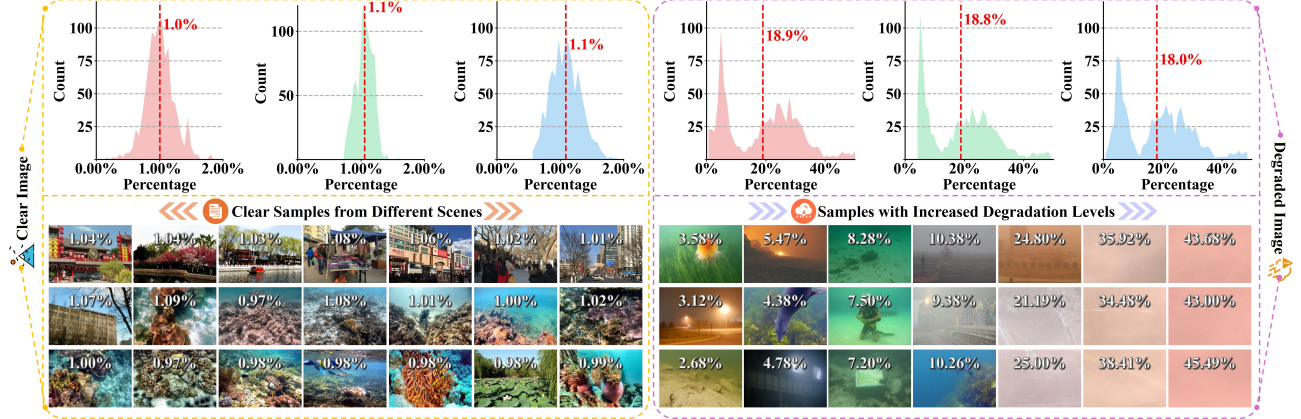


Figure 5. Statistical distributions of the percentages of low radial frequency components ( $<0.001$ ) in the  $\mathcal{R}$ ,  $\mathcal{G}$ , and  $\mathcal{B}$  channels for 1000 clear and 1000 degraded images. The horizontal axis represents the percentage of spectral magnitudes ( $<0.001$ ) in the total spectral magnitude, while the vertical axis indicates the number of images. The red dashed lines denote the mean values for each channel. The bottom row presents examples of clear and degraded images along with their corresponding low radial frequency percentages ( $<0.001$ ).

### 3.2. Frequency-Domain Priors

Degradations such as haze and sandstorms mainly affect the low-frequency components of images. Therefore, we conduct extensive statistical analyses to investigate the differences and correlations between the low-frequency components of degraded and clear images, based on which two frequency-domain priors are proposed to achieve adaptive frequency enhancement of degraded images.

The first frequency-domain prior is motivated by the observation that, in the frequency domain, the DC component of each channel in a clear image closely approximates the mean DC value across the three channels of its corresponding degraded image. To validate this prior, we conducted a statistical analysis on 1000 randomly selected degraded–clear image pairs from the UIEB [23] and RRSID [57] datasets. For each pair, we calculate the absolute difference between the DC component of each channel in the clear image and the mean DC value across the three channels of the corresponding degraded image. In Figure 4, the majority of image pairs (over 80%) exhibit absolute differences below 0.2, with some differences even approaching zero, indicating that the mean DC value of the degraded image across its three RGB channels is closely aligned with the DC component of each channel in the clear image.

The second frequency-domain prior is based on the observation that, for clear images, the percentage of low radial frequencies (below 0.001) within the total spectral magnitude is approximately 1%, with higher percentages indicating more severe degradation. To confirm the validity of this prior, we randomly collect 1000 high-quality clear images and 1000 degraded images, and perform statistical analyses of the percentage of low-frequency magnitudes ( $<0.001$ ) within the total spectral magnitude in each RGB channel. In Figure 5, the distributions of clear images are concentrated around 1%, whereas degraded images exhibit significantly

higher percentages. Furthermore, the examples of clear and degraded images, annotated with their corresponding low-frequency percentages ( $<0.001$ ), illustrate a direct correlation: percentages for clear scenes cluster near 1%, and increase with the severity of degradation.

## 4. Scene Recovery

### 4.1. Spatial-Domain Restoration

Based on our proposed spatial-domain prior, we project the inverted degraded image  $1 - \mathcal{I}(x)$  onto the spectral direction  $\mathcal{S}(x)$  to estimate the scene transmission:

$$t(x) = \frac{\sum_{\mathcal{C}} \langle \mathcal{S}_{\mathcal{C}}(x), 1 - \mathcal{I}_{\mathcal{C}}(x) \rangle \circ \mathcal{S}_{\mathcal{C}}(x)}{3}, \mathcal{C} \in \{\mathcal{R}, \mathcal{G}, \mathcal{B}\}, \quad (3)$$

where  $\langle \cdot, \cdot \rangle$  denotes the inner product.

To estimate the atmospheric light, we select the lowest 0.1% of the pixels in the transmission map and compute their average value in the observed image  $\mathcal{I}$  as  $\mathcal{A}$ . Once  $t$  and  $\mathcal{A}$  are obtained, the recovered image in the spatial domain is derived as:

$$\mathcal{J}(x) = (\mathcal{I}(x) - \mathcal{A}) / \mathcal{GF}(\max(t(x), t_{\min})) + \mathcal{A}, \quad (4)$$

where  $\mathcal{GF}$  denotes the guided filter [16], and  $t_{\min}$  is a lower bound set to the average of the lowest 5% of  $t(x)$ . For nighttime dehazing, the improved ASM with non-uniform atmospheric light [21] is employed.

### 4.2. Frequency-Domain Enhancement

To enhance the frequency components of degraded images, we design a simple yet effective adaptive mask derived from our proposed frequency-domain priors. Formally, the enhancement is expressed as follows:

$$\mathcal{E}_{\mathcal{C}}(x) = \mathcal{F}^{-1}(\mathcal{F}(\mathcal{I}_{\mathcal{C}})(x) \circ \mathcal{M}_{\mathcal{C}}(x)), \quad (5)$$





Figure 6. Visual comparisons with several state-of-the-art methods on five scene recovery tasks: daytime/nighttime dehazing, underwater image enhancement, and sandstorm/remote sensing image restoration.

where  $\mathcal{E}$  represents the enhanced result,  $\mathcal{F}(\cdot)$  and  $\mathcal{F}^{-1}(\cdot)$  denote the 2D Fourier transform (FFT) and its inverse, respectively. The adaptive mask  $\mathcal{M}_C(x)$  is defined as:

$$\mathcal{M}_C(x) = \alpha_C - e^{-(\rho(x)/\beta_C)^2}, \quad (6)$$

where  $\rho(x)$  denotes the normalized radial frequency, and  $\alpha_C$  and  $\beta_C$  are two parameters that control the magnitude of frequency enhancement, which are adaptively determined by our two frequency-domain priors.

Based on the first frequency-domain prior, we derive an equation associated with the DC components:

$$\mathcal{F}(\mathcal{E}_C)(0) = \frac{\sum_C \mathcal{F}(\mathcal{I}_C)(0)}{3} = \mu, C \in \{\mathcal{R}, \mathcal{G}, \mathcal{B}\}, \quad (7)$$

Combining Eq. (5) and Eq. (7) derives:

$$\mathcal{F}(\mathcal{E}_C)(0) = \mu = \mathcal{F}(\mathcal{I}_C)(0) \circ \mathcal{M}_C(0), \quad (8)$$

Given that the DC component corresponds to the zero radial frequency  $\rho(0) = 0$ , Eq. (6) gives:

$$\mathcal{M}_C(0) = \alpha_C - 1, \quad (9)$$

By substituting Eq. (9) into Eq. (8), we have:

$$\mu = \mathcal{F}(\mathcal{I}_C)(0) \circ (\alpha_C - 1), \quad (10)$$

Furthermore,  $\alpha_C$  is determined by rearranging Eq. (10):

$$\alpha_C = \mu / \mathcal{F}(\mathcal{I}_C)(0) + 1, \quad (11)$$

Using the second frequency-domain prior, we formulate the following energy function to estimate  $\beta_C$ , with the objective of bringing the percentage of low radial frequencies (below 0.001) close to 1%:

$$\arg \min_{\beta_C} \{\Phi(\mathcal{P}(\beta_C)) - 0.01\}, \quad (12)$$

where  $\Phi$  represents a function that calculates the percentage of low radial frequencies (below 0.001) and  $\mathcal{P}$  denotes the enhanced result associated with the parameter  $\beta_C$ . The above one-dimensional optimization problem can be efficiently solved using the fminbnd method.

### 4.3. Fusion

In order to effectively integrate the complementary information from the spatial-domain restored image, the frequency-enhanced image, and the input degraded image, a simple weighted fusion strategy is proposed. Specifically, all three images are first converted into the Lab color space to separately mitigate color distortion and enhance brightness. Subsequently, a weighted fusion is employed in the  $a$  and  $b$  channels as follows:

$$\mathcal{O}_{lab}^{a/b} = \mathcal{W}_{\mathcal{I}}^{a/b} \circ \mathcal{I}_{lab}^{a/b} + \mathcal{W}_{\mathcal{J}}^{a/b} \circ \mathcal{J}_{lab}^{a/b} + \mathcal{W}_{\mathcal{E}}^{a/b} \circ \mathcal{E}_{lab}^{a/b}, \quad (13)$$

where  $\mathcal{W}_{\mathcal{I}}^{a/b}$ ,  $\mathcal{W}_{\mathcal{J}}^{a/b}$ , and  $\mathcal{W}_{\mathcal{E}}^{a/b}$  are the weights of  $\mathcal{I}_{lab}^{a/b}$ ,  $\mathcal{J}_{lab}^{a/b}$ , and  $\mathcal{E}_{lab}^{a/b}$ , respectively. Leveraging the fundamental property that color-balanced images have near-zero means in the  $a$  and  $b$  channels of the Lab color space, we design the weights to fully utilize color-neutral information:

$$\mathcal{W}_{\mathcal{I}/\mathcal{J}/\mathcal{E}}^{a/b} = \frac{e^{-|\mathcal{M}_{\mathcal{I}/\mathcal{J}/\mathcal{E}}^{a/b}|}}{e^{-|\mathcal{M}_{\mathcal{I}}^{a/b}|} + e^{-|\mathcal{M}_{\mathcal{J}}^{a/b}|} + e^{-|\mathcal{M}_{\mathcal{E}}^{a/b}|}}, \quad (14)$$

where  $\mathcal{M}_{\mathcal{I}}^{a/b}$ ,  $\mathcal{M}_{\mathcal{J}}^{a/b}$ , and  $\mathcal{M}_{\mathcal{E}}^{a/b}$  are the mean values of the  $a/b$  color channels of  $\mathcal{I}$ ,  $\mathcal{J}$  and  $\mathcal{E}$ , respectively.

For the  $l$  channel, a discrete wavelet transform (DWT) is applied, in which the low-frequency component  $\mathcal{J}_{low}^l$  is retained and the high-frequency components are fused using a maximum-value strategy, as below:

$$\begin{cases} \mathcal{O}_{low}^l = \mathcal{J}_{low}^l, \\ \mathcal{O}_{high}^l = \max \{\mathcal{I}_{high}^l, \mathcal{J}_{high}^l, \mathcal{E}_{high}^l\}, \end{cases} \quad (15)$$

Finally,  $\mathcal{O}_{lab}$  is transformed back into the RGB color space to obtain the fused image. To further enhance brightness, we apply gamma correction and high dynamic range (HDR) compression as post-processing strategies.

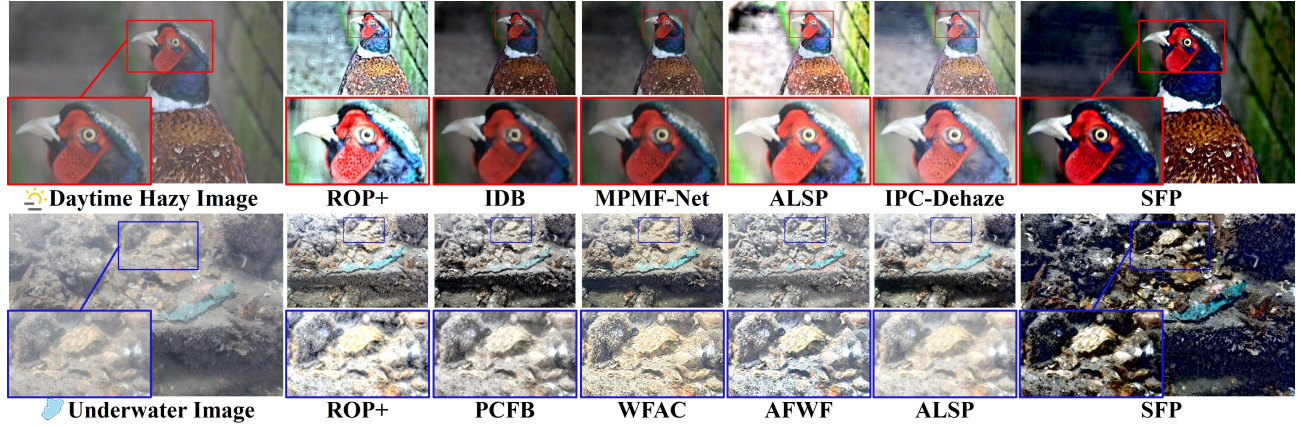


Figure 7. Visual comparisons with state-of-the-art methods on detail recovery for daytime dehazing and underwater image enhancement.

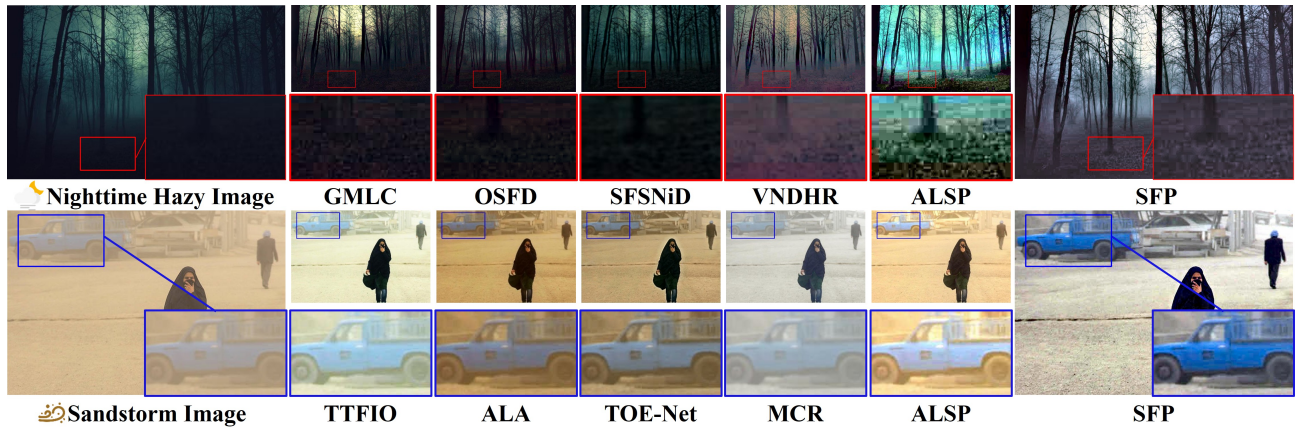


Figure 8. Visual comparisons with state-of-the-art methods on detail recovery for nighttime dehazing and sandstorm image restoration.

## 5. Experiments

### 5.1. Experimental Setting

**Implementation Details.** All experiments are conducted using MATLAB R2021b on a PC equipped with an AMD Ryzen 7 6800H processor and 16 GB of RAM. Notably, the proposed algorithm requires no large-scale datasets or extensive computational resources and operates autonomously without adjustable parameters, ensuring adaptability.

**Compared Methods.** To demonstrate the superiority of our proposed algorithm, we conduct extensive comparisons with 43 state-of-the-art (SOTA) approaches, including 35 single-task methods and 8 multi-task methods.

**Datasets.** For evaluation, we adopt five real-world datasets covering diverse degradation scenarios, including FTD [7] (500 real-world hazy images), NHRW [51] (150 real-world nighttime haze images), UIEB [23] (950 real-world underwater images), DID [4] (140 real-world sandstorm images), and RRSHID [57] (304 real-world remote sensing hazy images), for both quantitative and qualitative comparisons.

**Evaluation Metrics.** Four non-reference assessment metrics (NIMA [43], FADE [7], NIQE [37], and UCIQE [49]) are used to assess the visual quality of the recovered results.

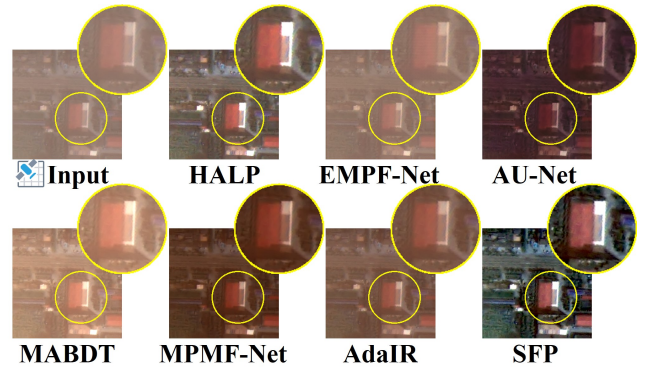


Figure 9. Visual comparisons with state-of-the-art methods on detail recovery for remote sensing image restoration.

### 5.2. Comparisons with State-of-the-Art Methods

**Visual Comparisons.** Figure 6 shows visual comparisons with SOTA methods across five real-world degradation scenarios. As illustrated, DehazeNet and SFSNiD fail to effectively recover scenes for real-world daytime/nighttime hazy conditions. Learning-based multi-task networks, such as MvKSR, ERA-Net, IDB, MPMF-Net, and AdaIR, exhibit limited generalization capabilities in real-world degra-



Table 1. Quantitative comparisons of 43 state-of-the-art methods on five real-world datasets across different scenarios. The top three results are highlighted in red, green, and blue, respectively.

Type	Method	Daytime Haze on FTD [7]		Method	Nighttime Haze on NHRW [51]		Method	Underwater on UIEB [23]		Method	Sandstorm on DID [4]		Method	Remote Sense on RRSID [57]	
		NIMA↑	FADE↓		NIMA↑	FADE↓		NIMA↑	UCIQE↑		NIQE↓	FADE↓		NIQE↓	NIMA↑
Single Task	DCP [15]	5.2225	<b>0.3897</b>	GMLC [26]	4.6971	<b>0.3115</b>	CBAF [3]	4.5436	24.8030	FBE [13]	4.0109	0.9096	SDCP [25]	7.5229	3.6602
	DehazeNet [5]	5.3073	0.7817	MRP [50]	4.7456	0.4414	HLRP [58]	4.3939	31.2309	TTFIO [1]	4.0512	1.0506	IDeRS [47]	7.3669	<b>3.7104</b>
	GCP [19]	4.8402	0.6502	FastMRP [50]	4.5458	0.3886	WWPF [53]	4.4912	30.8299	ALA [40]	4.0739	<b>0.8322</b>	HALP [18]	6.8655	3.4625
	SLP [30]	5.3433	<b>0.4897</b>	OSFD [51]	4.8570	<b>0.3804</b>	PCFB [52]	<b>4.7158</b>	<b>32.1515</b>	SBTE [22]	3.9031	0.9547	EMPF-Net [45]	14.1166	3.4513
	KA-Net [11]	5.1895	0.9164	URVM [35]	4.7484	0.4544	UDHTV [27]	4.6086	<b>32.3646</b>	OATF [4]	3.9072	0.9409	SDTE [29]	9.0225	3.6713
	DNMGDT [42]	5.0030	0.7407	SFSNiD [8]	3.9077	0.7641	AFWF [55]	4.2222	26.8035	TOE-Net [14]	3.9341	1.0142	AU-Net [10]	8.3588	3.3897
	IPC-Dehaze [12]	5.3342	0.8452	VNDHR [36]	4.7982	0.4910	WFAC [54]	<b>4.7379</b>	30.8520	MCR [2]	4.3374	1.9304	MABDT [39]	7.2939	3.3846
Multiple Tasks	ROP [31]	<b>5.3707</b>	0.8744	ROP [31]	4.9580	0.6842	ROP [31]	4.6067	31.5444	ROP [31]	<b>3.7897</b>	1.0910	ROP [31]	<b>6.2103</b>	<b>3.7166</b>
	ROP+ [32]	5.0983	0.5310	ROP+ [32]	4.5543	0.3838	ROP+ [32]	4.2856	31.1699	ROP+ [32]	<b>3.8428</b>	0.9162	ROP+ [32]	6.4571	3.4927
	MvKSR [48]	5.3021	1.4197	MvKSR [48]	5.0099	0.7440	MvKSR [48]	4.5302	23.5174	MvKSR [48]	4.3404	1.1085	MvKSR [48]	6.3273	3.4244
	ERA-Net [33]	5.3449	0.7818	ERA-Net [33]	<b>5.0498</b>	0.4333	ERA-Net [33]	4.6184	29.8718	ERA-Net [33]	4.2830	<b>0.7677</b>	ERA-Net [33]	7.3307	3.5211
	IDB [28]	4.2704	1.7605	IDB [28]	3.9662	0.7499	IDB [28]	4.0208	24.3363	IDB [28]	6.6331	1.2409	IDB [28]	9.0594	3.1124
	MPMF-Net [46]	5.1558	1.5129	MPMF-Net [46]	4.7543	0.8910	MPMF-Net [46]	4.4149	23.4699	MPMF-Net [46]	4.9124	1.0281	MPMF-Net [46]	7.7209	3.6701
	ALSP [17]	5.1667	1.0081	ALSP [17]	4.8583	0.5233	ALSP [17]	4.4955	29.9797	ALSP [17]	4.5979	0.8619	ALSP [17]	<b>5.9685</b>	3.4398
	AdaIR [9]	<b>5.3554</b>	1.1210	AdaIR [9]	<b>5.0286</b>	0.5152	AdaIR [9]	4.6267	25.1300	AdaIR [9]	4.5253	0.9953	AdaIR [9]	7.8480	3.3862
	SFP (Ours)	<b>5.4048</b>	<b>0.3226</b>	SFP (Ours)	<b>5.0551</b>	<b>0.3066</b>	SFP (Ours)	<b>4.7399</b>	<b>33.9766</b>	SFP (Ours)	<b>3.8680</b>	<b>0.7168</b>	SFP (Ours)	<b>6.3129</b>	<b>3.7384</b>

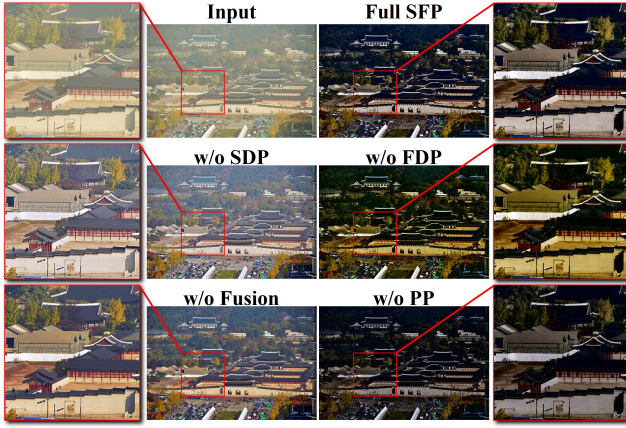


Figure 10. Visual comparison of our algorithm with different configurations in the ablation study.

dation scenes, primarily due to domain shifts between synthetic and real data. Prior-based scene recovery methods, such as ROP and ALSP, struggle to handle a wide range of degradations and often produce unnatural results. For instance, ROP yields overly bright result for remote sensing degraded images, and ALSP may over-enhance underwater images and be ineffective for sandstorm image restoration. In contrast, our SFP consistently achieves superior visual quality across all five degradation scenarios.

Figures 7-9 illustrate visual comparisons of detail recovery with other representative methods. From the zoomed-in patches, our SFP method recovers finer details and more vibrant colors than the competing SOTA methods. Overall, the proposed SFP method not only removes a wide range of degradations but also achieves scene recovery with natural colors and balanced contrast.

**Quantitative Comparisons.** Table 1 presents quantitative comparisons across five real-world degradation datasets. More specifically, the proposed SFP improves NIMA scores by roughly 0.63%, 0.1%, and 0.59% on FTD, NHRW, and

Table 2. Ablation study of individual modules on FTD dataset [7]

Component	SDP	FDP	Fusion	PP	NIMA↑	FADE↓
w/o SDP	✗	✓	✓	✓	5.3522	0.7401
w/o FDP	✓	✗	✓	✓	5.3855	0.3442
w/o Fusion	✓	✓	✗	✓	5.3779	0.6937
w/o PP	✓	✓	✓	✗	5.3486	0.3245
Ours	✓	✓	✓	✓	<b>5.4048</b>	<b>0.3226</b>

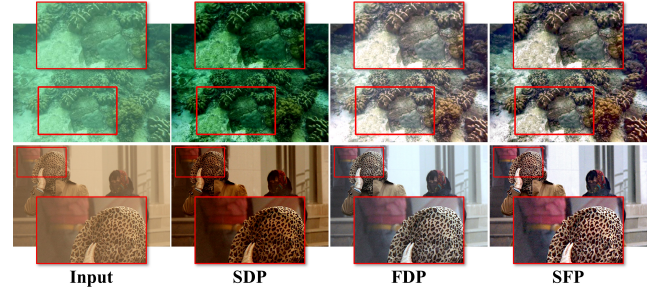


Figure 11. The recovered results obtained using SDP, FDP, and SFP, respectively.

RRSHID datasets, respectively. Additionally, SFP achieves gains of approximately 17.3%, 1.58%, and 6.66% in FADE scores on FTD, NHRW, and DID, respectively. Overall, the quantitative results highlight the superiority of our SFP across various real-world degradation scenarios.

### 5.3. Ablation Study

To verify the contribution of each module in our algorithm, the ablation study is performed on the FTD dataset [7].

**Effectiveness of Spatial-Domain Prior (SDP).** The SDP is designed to estimate the accurate transmission map for scene recovery by inverting the ASM, effectively removing degradations caused by scattering effects. In Figure 10, removing the SDP results in noticeable haze, with significant scattering artifacts remaining in the image. In addition, as demonstrated in Table 2, the removal of SDP leads to a noticeable decline in performance on FTD dataset, reflected



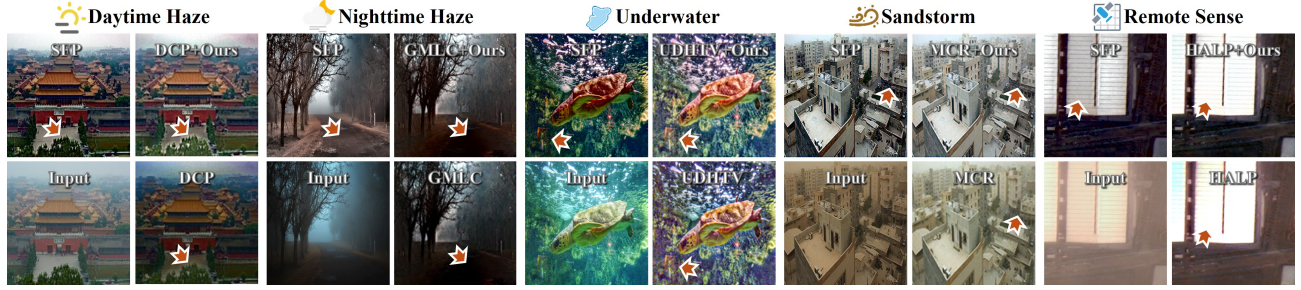


Figure 12. Plug-and-play integration of our algorithm with existing spatial-domain techniques for performance improvement.

in lower NIMA and FADE scores. Both visual and quantitative comparisons highlight the crucial role of the SDP in mitigating scattering-induced degradations.

**Effectiveness of Frequency-Domain Priors (FDP).** The FDP is proposed to construct an adaptive mask for frequency enhancement, which effectively mitigates the frequency loss caused by degradations. As illustrated in Figure 10, the recovered result without FDP may lead to unnatural colors, with significant color shifts evident in the zoomed-in region. Moreover, the objective metrics reveal a slight drop in performance after the removal of the FDP, confirming its role in maintaining color consistency.

**Effectiveness of Fusion.** In Figure 11, the SDP effectively removes scattering-induced degradations, preserving fine image details, while the FDP corrects color distortions by enhancing the frequency components. Each prior, SDP and FDP, contributes distinct advantages, which are effectively combined through our fusion strategy. As shown, the results obtained with SFP significantly outperform those achieved using either of the individual priors.

To further validate the effectiveness of our weighted fusion strategy, we compare it with a naive fusion approach, which simply averages the pixel values of the fused images. The naive fusion approach (denoted as ‘w/o fusion’ in Figure 10) fails to leverage the distinct advantages of the individual priors, resulting in images with reduced detail and contrast. In contrast, our weighted fusion strategy effectively integrates the strengths of both the SDP and FDP, yielding sharper details, enhanced contrast, and vivid colors, as indicated by the quantitative metrics in Table 2.

**Effectiveness of Postprocessing.** The postprocessing (PP) step includes gamma correction and HDR compression to further adjust the overall luminance and enhance the contrast. Figure 10 and Table 2 show that the postprocessing further improves the visual quality of the recovered images.

**Effectiveness of Plug-and-Play Property.** In Figure 12, the SDP can be seamlessly replaced with any existing spatial-domain methods, such as DCP, GMLC UDHTV, MCR, and HALP, significantly improving their performance for the respective scene recovery tasks. This plug-and-play property highlights the flexibility of our approach, allowing seamless integration with various spatial-domain-

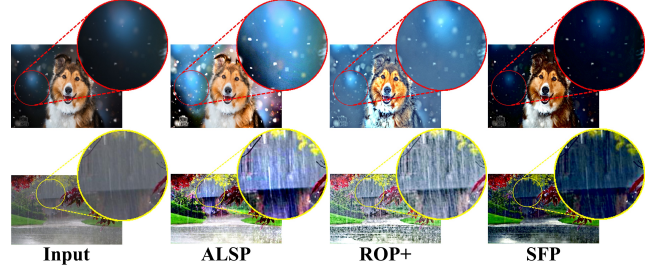


Figure 13. Failure cases of the proposed SFP for rainy and snowy degradation scenarios.

based task-specific methods to boost performance. Moreover, our SFP outperforms these alternative spatial-domain methods, further verifying the superiority of our SDP.

#### 5.4. Limitations

While effective for various real-world degradation scenarios, our algorithm struggles with high-frequency degradations, such as rain streaks and snow particles. In Figure 13, although our algorithm improves the overall clarity of degraded images, artifacts caused by rain streaks and snow particles remain. This limitation arises because our SDP-based model is not applicable to these types of degradations, and the frequency-domain priors primarily focus on low-frequency degradations affected by haze and sandstorms.

## 6. Conclusion

This paper proposes SFP, a novel real-world scene recovery framework that integrates spatial and frequency priors. In the spatial domain, we propose a prior based on the projection principle of the inverse degraded image along its spectral direction to estimate the scene transmission, thereby removing scattering effects. In the frequency domain, we propose two priors by analyzing low-frequency disparities between clear and degraded images, to construct a mask to adaptively enhance frequency components. Unlike previous priors that typically focus on a single domain, SFP jointly exploits degradation cues from both spatial and frequency perspectives, enabling more reliable scene recovery. Experiments demonstrate that our SFP outperforms state-of-the-art methods across diverse degradation scenarios in both qualitative and quantitative evaluations.

## References

- [1] Zohair Al-Ameen. Visibility enhancement for images captured in dusty weather via tuned tri-threshold fuzzy intensification operators. *International Journal of Intelligent Systems and Applications*, 8(8):10, 2016. 7
- [2] Zohair Al-Ameen. Increasing the lucidity of sandstorm images using a multistep color reparation algorithm. *Signal, Image and Video Processing*, 18(11):8005–8017, 2024. 7
- [3] Codruta O Ancuti, Cosmin Ancuti, Christophe De Vleeschouwer, and Philippe Bekaert. Color balance and fusion for underwater image enhancement. *IEEE Trans. Image Process.*, 27(1):379–393, 2018. 7
- [4] Ako Bartani, Alireza Abdollahpour, Mohsen Ramezani, and Fardin Akhlaghian Tab. An adaptive optic-physic based dust removal method using optimized air-light and transfer function. *Multimedia Tools and Applications*, 81(23):33823–33849, 2022. 6, 7
- [5] Bolun Cai, Xiangmin Xu, Kui Jia, Chunmei Qing, and Dacheng Tao. DehazeNet: An end-to-end system for single image haze removal. *IEEE Trans. Image Process.*, 25(11):5187–5198, 2016. 1, 2, 7
- [6] I-Hsiang Chen, Wei-Ting Chen, Yu-Wei Liu, Yuan-Chun Chiang, Sy-Yen Kuo, and Ming-Hsuan Yang. Unirestore: Unified perceptual and task-oriented image restoration model using diffusion prior. In *CVPR*, pages 17969–17979, 2025. 1, 2
- [7] Lark Kwon Choi, Jaehye You, and Alan Conrad Bovik. Referenceless prediction of perceptual fog density and perceptual image defogging. *IEEE Trans. Image Process.*, 24(11):3888–3901, 2015. 6, 7
- [8] Xiaofeng Cong, Jie Gui, Jing Zhang, Junming Hou, and Hao Shen. A semi-supervised nighttime dehazing baseline with spatial-frequency aware and realistic brightness constraint. In *CVPR*, pages 2631–2640, 2024. 1, 2, 7
- [9] Yuning Cui, Syed Waqas Zamir, Salman Khan, Alois Knoll, Mubarak Shah, and Fahad Shahbaz Khan. Adair: Adaptive all-in-one image restoration via frequency mining and modulation. In *ICLR*, pages 57335–57356, 2025. 1, 2, 3, 7
- [10] Yang Du, Jun Li, Qinghong Sheng, Yuxin Zhu, Bo Wang, and Xiao Ling. Dehazing network: Asymmetric unet based on physical model. *IEEE Transactions on Geoscience and Remote Sensing*, 62:1–12, 2024. 7
- [11] Yuxin Feng, Long Ma, Xiaozhe Meng, Fan Zhou, Risheng Liu, and Zhuo Su. Advancing real-world image dehazing: Perspective, modules, and training. *IEEE Trans. Pattern Anal. Mach. Intell.*, 46(12):9303–9320, 2024. 2, 7
- [12] Jiayi Fu, Siyu Liu, Zikun Liu, Chun-Le Guo, Hyunhee Park, Ruiqi Wu, Guoqing Wang, and Chongyi Li. Iterative predictor-critic code decoding for real-world image dehazing. In *CVPR*, pages 12700–12709, 2025. 1, 2, 7
- [13] Xueyang Fu, Yue Huang, Delu Zeng, Xiao-Ping Zhang, and Xinghao Ding. A fusion-based enhancing approach for single sandstorm image. In *2014 IEEE 16th international workshop on multimedia signal processing (MMSP)*, pages 1–5. IEEE, 2014. 7
- [14] Yuan Gao, Wenyu Xu, and Yuxu Lu. Let you see in haze and sandstorm: Two-in-one low-visibility enhancement network. *IEEE Transactions on Instrumentation and Measurement*, 72:1–12, 2023. 7
- [15] Kaiming He, Jian Sun, and Xiaoou Tang. Single image haze removal using dark channel prior. *IEEE Trans. Pattern Anal. Mach. Intell.*, 33(12):2341–2353, 2011. 1, 2, 3, 7
- [16] Kaiming He, Jian Sun, and Xiaoou Tang. Guided image filtering. *IEEE Trans. Pattern Anal. Mach. Intell.*, 35(6):1397–1409, 2013. 4
- [17] Lei He, Zunhui Yi, Jinshi Liu, Chaoyang Chen, Ming Lu, and Zhipeng Chen. Alsp+: fast scene recovery via ambient light similarity prior. *IEEE Trans. Image Process.*, 34:4470–4484, 2025. 1, 2, 7
- [18] Yufeng He, Cuili Li, and Xu Li. Remote sensing image dehazing using heterogeneous atmospheric light prior. *IEEE Access*, 11:18805–18820, 2023. 7
- [19] Mingye Ju, Can Ding, Y Jay Guo, and Dengyin Zhang. IDGCP: Image dehazing based on gamma correction prior. *IEEE Trans. Image Process.*, 29:3104–3118, 2019. 1, 2, 3, 7
- [20] Mingye Ju, Can Ding, Charles A Guo, Wenqi Ren, and Dacheng Tao. IDRLP: Image dehazing using region line prior. *IEEE Trans. Image Process.*, 30:9043–9057, 2021. 1, 2, 3
- [21] Mingye Ju, Can Ding, Wenqi Ren, Yi Yang, Dengyin Zhang, and Y Jay Guo. Ide: Image dehazing and exposure using an enhanced atmospheric scattering model. *IEEE Trans. Image Process.*, 30:2180–2192, 2021. 4
- [22] Se Eun Kim, Tae Hee Park, and Il Kyu Eom. Fast single image dehazing using saturation based transmission map estimation. *IEEE Trans. Image Process.*, 29:1985–1998, 2020. 7
- [23] Chongyi Li, Chunle Guo, Wenqi Ren, Runmin Cong, Junhui Hou, Sam Kwong, and Dacheng Tao. An underwater image enhancement benchmark dataset and beyond. *IEEE Trans. Image Process.*, 29:4376–4389, 2019. 4, 6, 7
- [24] Chong-Yi Li, Ji-Chang Guo, Run-Min Cong, Yan-Wei Pang, and Bo Wang. Underwater image enhancement by dehazing with minimum information loss and histogram distribution prior. *IEEE Trans. Image Process.*, 25(12):5664–5677, 2016. 1
- [25] Jiayuan Li, Qingwu Hu, and Mingyao Ai. Haze and thin cloud removal via sphere model improved dark channel prior. *IEEE Geoscience and Remote Sensing Letters*, 16(3):472–476, 2018. 7
- [26] Yu Li, Robby T Tan, and Michael S Brown. Nighttime haze removal with glow and multiple light colors. In *ICCV*, pages 226–234, 2015. 7
- [27] Yuemei Li, Guojia Hou, Peixian Zhuang, and Zhenkuan Pan. Dual high-order total variation model for underwater image restoration. *IEEE Transactions on Multimedia*, 2025. 7
- [28] Zhan Li, Wenqing Kuang, Bir Bhanu, Yifan Deng, Yihang Chen, and Kangkang Xu. Low-visibility scene enhancement by isomorphic dual-branch framework with attention learning. *IEEE Transactions on Intelligent Transportation Systems*, 2025. 1, 2, 7
- [29] Zheng Liang, Rui Ruan, Chuanjian Wang, and Peixian Zhuang. Single image quality improvement via joint local structure dehazing and local texture enhancement. *IEEE Transactions on Geoscience and Remote Sensing*, 2024. 7

- [30] Pengyang Ling, Huaian Chen, Xiao Tan, Yi Jin, and Enhong Chen. Single image dehazing using saturation line prior. *IEEE Trans. Image Process.*, 32:3238–3253, 2023. 1, 2, 3, 7
- [31] Jun Liu, Wen Liu, Jianing Sun, and Tiejong Zeng. Rank-one prior: Toward real-time scene recovery. In *Proceedings of the IEEE/CVF conference on computer vision and pattern recognition*, pages 14802–14810, 2021. 1, 2, 7
- [32] Jun Liu, Ryan Wen Liu, Jianing Sun, and Tiejong Zeng. Rank-one prior: Real-time scene recovery. *IEEE Trans. Pattern Anal. Mach. Intell.*, 45(7):8845–8860, 2023. 1, 2, 7
- [33] Ryan Wen Liu, Yuxu Lu, Yuan Gao, Yu Guo, Wenqi Ren, Fenghua Zhu, and Fei-Yue Wang. Real-time multi-scene visibility enhancement for promoting navigational safety of vessels under complex weather conditions. *IEEE Transactions on Intelligent Transportation Systems*, 2024. 1, 2, 7
- [34] Ye Liu, Lei Zhu, Shunda Pei, Huazhu Fu, Jing Qin, Qing Zhang, Liang Wan, and Wei Feng. From synthetic to real: Image dehazing collaborating with unlabeled real data. In *ACM MM*, pages 50–58, 2021. 3
- [35] Yun Liu, Zhongsheng Yan, Jing Tan, and Yuche Li. Multi-purpose oriented single nighttime image haze removal based on unified variational retinex model. *IEEE Trans. Circuits Syst. Video Technol.*, 33(4):1643–1657, 2023. 2, 7
- [36] Yun Liu, Xinran Wang, Enping Hu, Anzhi Wang, Babak Shiri, and Weisi Lin. Vndhr: Variational single nighttime image dehazing for enhancing visibility in intelligent transportation systems via hybrid regularization. *IEEE Transactions on Intelligent Transportation Systems*, 2025. 2, 7
- [37] Anish Mittal, Rajiv Soundararajan, and Alan C Bovik. Making a “completely blind” image quality analyzer. *IEEE Signal processing letters*, 20(3):209–212, 2013. 6
- [38] S. G. Narasimhan and S. K. Nayar. Vision and the atmosphere. *Int. J. Comput. Vis.*, 48:233–254, 2002. 3
- [39] Jin Ning, Jie Yin, Fei Deng, and Lianbin Xie. Mabdt: Multi-scale attention boosted deformable transformer for remote sensing image dehazing. *Signal Processing*, 229:109768, 2025. 1, 2, 7
- [40] Yan-Tsung Peng, Zhihui Lu, Fan-Chieh Cheng, Yalun Zheng, and Shih-Chia Huang. Image haze removal using airlight white correction, local light filter, and aerial perspective prior. *IEEE Transactions on Circuits and Systems for Video Technology*, 30(5):1385–1395, 2019. 7
- [41] Wenqi Ren, Si Liu, Hua Zhang, Jinshan Pan, Xiaochun Cao, and Ming-Hsuan Yang. Single image dehazing via multi-scale convolutional neural networks. In *ECCV*, pages 154–169. Springer, 2016. 1
- [42] Yanzhao Su, Nian Wang, Zhigao Cui, Yanping Cai, Chuan He, and Aihua Li. Real scene single image dehazing network with multi-prior guidance and domain transfer. *IEEE Transactions on Multimedia*, 2025. 1, 2, 7
- [43] Hossein Talebi and Peyman Milanfar. Nima: Neural image assessment. *IEEE Trans. Image Process.*, 27(8):3998–4011, 2018. 6
- [44] Jeya Maria Jose Valanarasu, Rajeev Yasarla, and Vishal M Patel. Transweather: Transformer-based restoration of images degraded by adverse weather conditions. In *CVPR*, pages 2353–2363, 2022. 1
- [45] Yuanbo Wen, Tao Gao, Jing Zhang, Ziqi Li, and Ting Chen. Encoder-free multi-axis physics-aware fusion network for remote sensing image dehazing. *IEEE Transactions on Geoscience and Remote Sensing*, 61:1–15, 2023. 2, 7
- [46] Yuanbo Wen, Tao Gao, Jing Zhang, Ziqi Li, and Ting Chen. Multi-axis prompt and multi-dimension fusion network for all-in-one weather-degraded image restoration. In *AAAI*, pages 8323–8331, 2025. 1, 2, 3, 7
- [47] Long Xu, Dong Zhao, Yihua Yan, Sam Kwong, Jie Chen, and Ling-Yu Duan. Iders: Iterative dehazing method for single remote sensing image. *Information Sciences*, 489:50–62, 2019. 7
- [48] Wenyu Xu, Dong Yang, Yuan Gao, Yuxu Lu, Jingming Zhang, and Yu Guo. Mvksr: Multi-view knowledge-guided scene recovery for hazy and rainy degradation. *IEEE Transactions on Instrumentation and Measurement*, 2024. 1, 2, 7
- [49] Miao Yang and Arcot Sowmya. An underwater color image quality evaluation metric. *IEEE Trans. Image Process.*, 24(12):6062–6071, 2015. 6
- [50] Jing Zhang, Yang Cao, Shuai Fang, Yu Kang, and Chang Wen Chen. Fast haze removal for nighttime image using maximum reflectance prior. In *CVPR*, pages 7418–7426, 2017. 1, 2, 7
- [51] Jing Zhang, Yang Cao, Zheng-Jun Zha, and Dacheng Tao. Nighttime dehazing with a synthetic benchmark. In *ACM MM*, pages 2355–2363, 2020. 6, 7
- [52] Weidong Zhang, Qingmin Liu, Yikun Feng, Lei Cai, and Peixian Zhuang. Underwater image enhancement via principal component fusion of foreground and background. *IEEE Transactions on Circuits and Systems for Video Technology*, 34(11):10930–10943, 2024. 7
- [53] Weidong Zhang, Ling Zhou, Peixian Zhuang, Guohou Li, Xipeng Pan, Wenyi Zhao, and Chongyi Li. Underwater image enhancement via weighted wavelet visual perception fusion. *IEEE Transactions on Circuits and Systems for Video Technology*, 34(4):2469–2483, 2024. 7
- [54] Weidong Zhang, Qingmin Liu, Huimin Lu, Jianping Wang, and Jing Liang. Underwater image enhancement via wavelet decomposition fusion of advantage contrast. *IEEE Transactions on Circuits and Systems for Video Technology*, 2025. 7
- [55] Weidong Zhang, Muzi Wang, Peixian Zhuang, and Dahai Liu. Underwater image enhancement via advantage feature weighted fusion. *IEEE Transactions on Circuits and Systems for Video Technology*, 2025. 7
- [56] Qingsong Zhu, Jiaming Mai, and Ling Shao. A fast single image haze removal algorithm using color attenuation prior. *IEEE Trans. Image Process.*, 24(11):3522–3533, 2015. 1, 2, 3
- [57] Zeng-Hui Zhu, Wei Lu, Si-Bao Chen, Chris HQ Ding, Jin Tang, and Bin Luo. Real-world remote sensing image dehazing: Benchmark and baseline. *IEEE Transactions on Geoscience and Remote Sensing*, 2025. 4, 6, 7
- [58] Peixian Zhuang, Jiamin Wu, Fatih Porikli, and Chongyi Li. Underwater image enhancement with hyper-laplacian reflectance priors. *IEEE Trans. Image Process.*, 31:5442–5455, 2022. 1, 2, 7